Volume 58
Number 31
21 April 2022
Pages 4803–4920

ChemComm

Chemical Communications

rsc.li/chemcomm

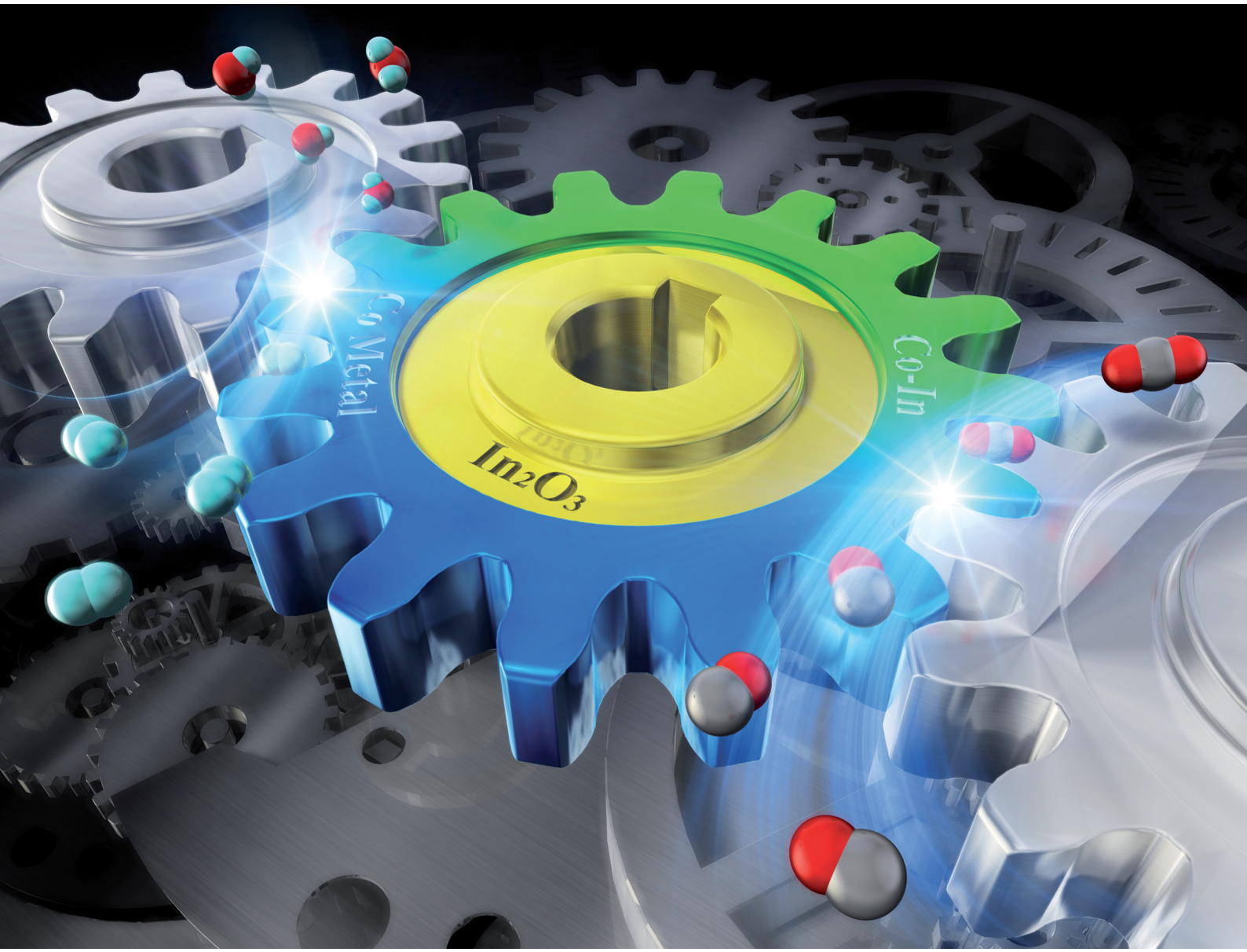

ISSN 1359-7345

ROYAL SOCIETY OF CHEMISTRY

COMMUNICATION

Yasushi Sekine *et al.*

Efficient CO_2 conversion to CO using chemical looping over Co–In oxide

ChemComm

COMMUNICATION

View Article Online
View Journal | View Issue

Cite this: *Chem. Commun.*, 2022, **58**, 4837

Received 12th January 2022,
Accepted 3rd March 2022

DOI: 10.1039/d2cc00208f

rsc.li/chemcomm

Efficient CO_2 conversion to CO using chemical looping over Co–In oxide†

Jun-Ichiro Makiura,[a] Sota Kakihara,[a] Takuma Higo,[a] Naoki Ito,[b] Yuichiro Hirano[b] and Yasushi Sekine *[a]

CO_2 conversion to CO by reverse water-gas shift using chemical looping (RWGS-CL) can be conducted at lower temperatures (*ca.* 723–823 K) than the conventional catalytic RWGS (>973 K), and has been attracting attention as an efficient process for CO production from CO_2. In this study, Co–In_2O_3 was developed as an oxygen storage material (OSM) that can realize an efficient RWGS-CL process. Co–In_2O_3 showed a high CO_2 splitting rate in the mid-temperature range (723–823 K) compared with previously reported materials and had high durability through redox cycles. Importantly, the maximum CO_2 conversion in the CO_2 splitting step (*ca.* 80%) was much higher than the equilibrium conversion of catalytic RWGS in the mid-temperature range, indicating that Co–In_2O_3 is a suitable OSM for the RWGS-CL process.

Limiting anthropogenic global warming to a specific level requires reaching at least net zero CO_2 emissions.[1,2] For this purpose, syntheses of liquid fuels using renewable electricity and captured CO_2, which are, respectively, designated as Sun-to-Fuel (STF) and Power-to-Liquid (PtL),[3] have been proposed as technologies to replace fossil fuels by carbon-neutral energy resources. The CO_2-based fuels produced by PtL processes can supply renewable energy to the transportation sector.[4,5] One feasible route for PtL processing from captured CO_2 is the Fischer–Tropsch (FT) method.[6] Nevertheless, technologies for direct synthesis from CO_2 are currently in an early stage. Consequently, in the near future, CO converted from captured CO_2 might be a useful intermediate for PtL fuel processing. Reverse water-gas shift (RWGS) is a representative method of converting CO_2 to CO. It is an endothermic equilibrium-limited reaction.[7]

$$CO_2 + H_2 \leftrightarrow CO + H_2O \quad \Delta H^0_{298} = 42.1 \text{ kJ mol}^{-1} \qquad (1)$$

Mallapragada *et al.* estimated that the route consisting of RWGS followed by FT synthesis is a more efficient route for STF than other routes such as biomass gasification, algae-derived oils, and direct photosynthesis.[8] However, conventional catalytic RWGS requires high reaction temperatures and separation of gaseous products to achieve high conversion and a suitable H_2/CO ratio syngas. Moreover, side reactions (eqn (2) and (3)) also occur, which complicate the separation of the outlet gas and reduce the process efficiency.[7]

$$CO + 3H_2 \leftrightarrow CH_4 + H_2O \quad \Delta H^0_{298} = -206.5 \text{ kJ mol}^{-1} \qquad (2)$$

$$CO_2 + 4H_2 \leftrightarrow CH_4 + 2H_2O \quad \Delta H^0_{298} = -165.0 \text{ kJ mol}^{-1} \qquad (3)$$

Reverse water-gas shift *via* chemical looping (RWGS-CL) can overcome the shortcomings of conventional catalytic processing.[9–12] In RWGS-CL, CO_2 is converted to CO in a separated redox reaction on oxygen storage materials (OSMs), as shown in eqn (4) and (5).

$$\text{Reduction of OSM: } MO_x + \delta H_2 \leftrightarrow MO_{x-\delta} + \delta H_2O \qquad (4)$$

$$\text{Oxidation of OSM: } MO_{x-\delta} + \delta CO_2 \leftrightarrow MO_x + \delta CO \qquad (5)$$

In this process, CH_4 formation is avoided because CO/CO_2 and H_2/H_2O flows are separated. Therefore, RWGS-CL processes present benefits of driving the reaction toward CO production and of simplifying gas separation. A study of solar-to-syngas process efficiency revealed that RWGS-CL processing can reduce the energy demand for separation by 77% compared to conventional catalytic RWGS processing.[9] The redox performance of the OSM is an important factor that makes this process feasible. Recently reported results have shown that Cu-modified In_2O_3 (Cu–In_2O_3) exhibits a higher CO_2 splitting rate[12] than earlier reported OSMs such as perovskite-type oxides[11,13–19] and Fe-based oxides[20–26] at low temperatures (673–823 K). Actually, RWGS-CL on Cu–In_2O_3 proceeds by the redox of In(0) ⇆ In(III) with the formation and decomposition of a Cu–In alloy. The high CO_2 splitting rate on Cu–In_2O_3 is attributable to fast migration of oxide ions in the Cu–In alloy and the preferential oxidation of the interface of alloy–In_2O_3. In terms of the CO_2 decomposition rate, Cu–In_2O_3 is a promising

[a] *Department of Applied Chemistry, Waseda University, 3-4-1, Okubo, Shinjuku, Tokyo, 169-8555, Japan. E-mail: ysekine@waseda.jp*
[b] *ENEOS, 1-1-2 Otemachi, Chiyoda, Tokyo 100 8162, Japan*

† Electronic supplementary information (ESI) available. See DOI: 10.1039/d2cc00208f

OSM, but it presents issues related to durability over numerous cycles. In addition, because of its high reducibility, the rate of reverse reaction in eqn (5) is also high, resulting in a low CO concentration ($CO/CO + CO_2$) in the product gas.

Here we propose a novel material for this purpose. The most desirable OSM for this purpose was found to be Co-modified In_2O_3 ($Co–In_2O_3$). In fact, $Co–In_2O_3$ showed a higher CO_2 splitting rate, even at low temperatures (723–823 K) under an atmosphere with high CO concentration.

To elucidate the mechanism of CO_2 splitting on this OSM, various characterizations were undertaken using powder X-ray diffraction (XRD), scanning transmission electron microscopy with energy-dispersive X-ray spectrometry (STEM-EDX) and *in situ* X-ray absorption fine structure (XAFS) measurements.

Co-supported indium-based oxides used for this study were prepared using a complex polymerization method and an impregnation method. The procedures are described in the ESI.† The procedures for redox tests, *i.e.* CO_2 splitting and regeneration, are also described in the ESI.† The series of reduction and oxidation steps was defined as one cycle for isothermal RWGS-CL. The amount of reduction and oxidation (redox) was defined as the amount of oxygen atoms released or backfilled in each step. The maximum CO_2 conversion of the oxidation reaction (eqn (5)) was also evaluated. Electronic states of samples were evaluated using *in situ* In and Co K-edge X-ray absorption fine structure (XAFS) spectroscopy at the BL14B2 beamline of SPring-8 in Japan. XAFS measurements were conducted in transmission mode. Details of these characterisations are described in the ESI.†

First, we conducted screening tests for oxides that achieve high RWGS-CL performance. Subsequently, Co–In oxide ($Co–In_2O_3$) was developed. Fig. 1 presents a comparison of the CO_2 splitting rate with previously reported materials (please see also ESI†). The $Co–In_2O_3$ showed very high oxidation rates of 127.6, 191.0, 280.2, 365.7, and 429.5 μmol min^{-1} g^{-1}, respectively, in the middle-temperature and low-temperature ranges of 723, 748, 773, 798, and 823 K, exceeding those of previously reported perovskite oxides,[11,13–19] Fe-based oxides,[20–26] and In-based oxides.[12] Therefore, it is considered that $Co–In_2O_3$ is kinetically the most promising oxide for RWGS-CL.

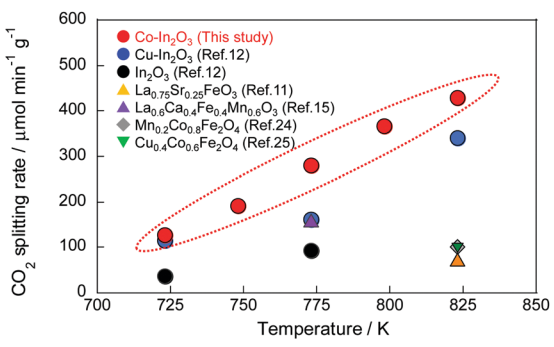

Fig. 1 Comparison of average CO_2 splitting rates on $Co–In_2O_3$ (this study) and on various oxides in earlier reports: The purple triangle plot represents the maximum CO_2 conversion rate during temperature-programmed oxidation by CO_2 over $La_{0.6}Ca_{0.4}Fe_{0.4}Mn_{0.6}O_3$[15].

The results of RWGS-CL cycling tests for 10 cycles by $Co–In_2O_3$ are presented in Fig. 2. The detailed RWGS-CL results and the confirmation of the outlet gas in the re-oxidation step are shown in Table S1 and Fig. S1 (ESI†). $Co–In_2O_3$ showed a reduction amount of 6.39 mmol g^{-1} and oxidation amount of 2.73 mmol g^{-1} in the first cycle and a redox amount of 3.25 ± 0.05 mmol g^{-1} after the second cycle. The amount of reduction that was not backfilled by CO_2 in the first cycle was found to be the reduction of Co by crystal structure analysis, as discussed in detail later, which indicates that in $Co–In_2O_3$, the redox of Co is not involved in the reaction after the reduction of the first cycle. The only redox species is indium. In contrast to the high redox performance of $Co–In_2O_3$, In_2O_3 reportedly has a redox amount of about 1.64 mmol g^{-1} and an oxidation rate of 93.4 μmol min^{-1} g^{-1} at 773 K.[12] Although the redox species is indium in both oxides, $Co–In_2O_3$ shows higher redox capacity and a higher oxidation rate than those of In_2O_3. Consequently, the results indicate that Co can enhance the redox performance of indium. Moreover, in terms of stability, $Cu–In_2O_3$, which has high RWGS-CL performance and the same redox mechanism as $Co–In_2O_3$, shows an oxidation rate of 161.8 μmol min^{-1} g^{-1} in the first cycle, but the rate decreases to 85.5 μmol min^{-1} g^{-1} in the fifth cycle.[12] However, $Co–In_2O_3$ showed an oxidation rate of 293.2 μmol min^{-1} g^{-1} in the second cycle, and still shows a high oxidation rate of 281.8 μmol min^{-1} g^{-1} in the tenth cycle, with no noticeable decrease in the rate, maintaining high stability. These results demonstrate that Co can improve the redox performance of indium, especially its oxidation performance, and can stabilize the redox of indium.

Next, the maximum CO_2 conversion in the oxidation step of $Co–In_2O_3$ and previously reported In-based oxides was compared with the equilibrium conversion of conventional RWGS.[27] The results are depicted in Fig. 3. Actually, $Cu–In_2O_3$, which is reported to have high redox kinetics, was found to be thermodynamically disadvantageous when compared to conventional RWGS. This finding indicated that $Cu–In_2O_3$ as unsuitable for industrial applications. Regarding In_2O_3, a maximum CO_2 conversion of 70–90% was achieved in the medium temperature region (at 673 K), which is much higher than the equilibrium conversion

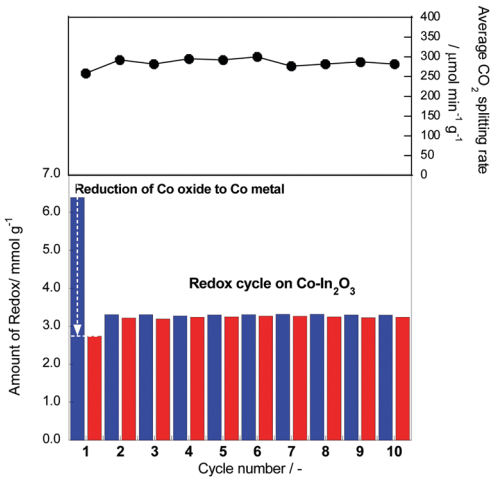

Fig. 2 RWGS-CL stability test for $Co–In_2O_3$.

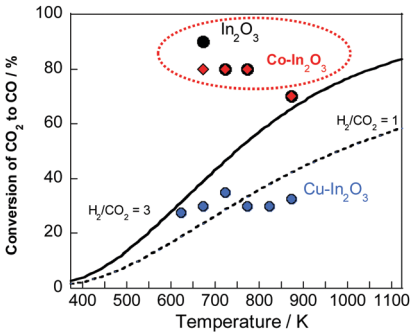

Fig. 3 Comparison between equilibrium conversion of conventional RWGS and maximum CO_2 conversion of RWGS-CL materials during the oxidation step.

of conventional RWGS. Nevertheless, concern persists that In(0), which is derived from the reduction of In_2O_3, is liquefied in the medium temperature region (at 673 K) because of its low melting point. This issue engenders challenges for the industrialization of the RWGS-CL process. However, Co–In_2O_3 also achieved a high maximum CO_2 conversion of 70–80% in the medium temperature region, while suppressing the melting of indium because the redox of indium progresses with the formation and decomposition of Co–In alloy (as discussed later) with a high melting point.[28] To summarize the discussion presented above, Co–In_2O_3 can improve the redox kinetics of indium and can achieve high stability, while maintaining the maximum CO_2 conversion. Additionally, compared to materials reported earlier, Co–In_2O_3 has higher performance and is an industrially more promising material.

Next, the structural and electronic states of the Co–In_2O_3 in RWGS-CL were evaluated using XRD, STEM-EDX, and XAFS measurements. In the XRD of the as-prepared Co–In_2O_3 (see Fig. S2 in ESI†), the diffraction peaks of Co_3O_4 and In_2O_3 were observed, respectively, with no peak shift in each representative diffraction peak, indicating that the complexation of Co and In did not occur. The SEM image (Fig. S3 in ESI†) showed particles of several hundred nanometres. The EDS image showed non-uniform dispersion of Co species and uniform dispersion of In species. The XRD profile of the reduced sample (Fig. S2, ESI†) shows diffraction peaks of Co–In alloy ($CoIn_2$), Co metal, and In_2O_3. The results demonstrated that a part of the Co reduced by hydrogen formed an alloy with indium, which was also reduced. The XRD profile of the re-oxidized sample (Fig. S2, ESI†) showed diffraction peaks of Co metal and In_2O_3, indicating that CO_2 oxidizes only indium in the Co–In alloy and not in Co metal. In other words, the RWGS-CL in the Co–In_2O_3 is established by the redox of indium with the formation and decomposition of the Co–In alloy. The SEM images obtained after reduction and re-oxidation (Fig. S3, ESI†) showed particles of several thousand nanometres in size. The EDS images showed sparsely and heterogeneously dispersed Co on the In species. The Co species dispersed sparsely and heterogeneously on the indium species were regarded as involved in the alloy formation with indium.

The Co K-edge and In K-edge XANES spectra of Co–In_2O_3 during RWGS-CL are shown in Fig. 4. Several spectral changes at the In K-edge (Fig. 4(A and B)) represent the redox of indium

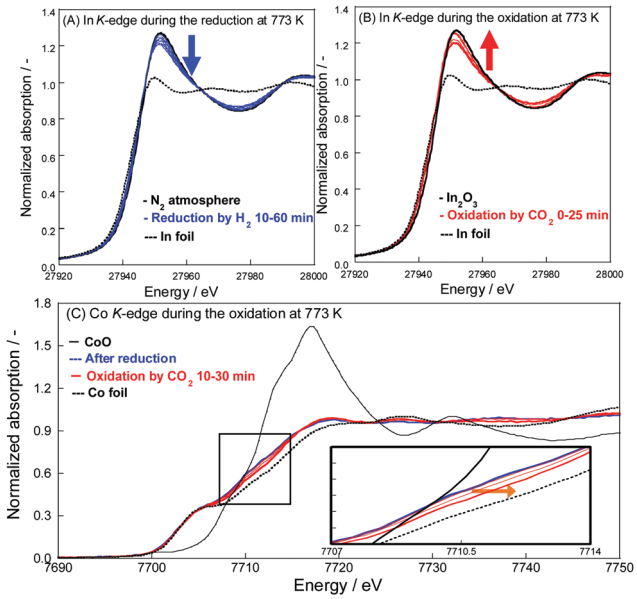

Fig. 4 The XANES spectra of Co–In_2O_3 during (A) H_2 reduction and (B) CO_2 oxidation on In K-edge, and (C) H_2 reduction and CO_2 oxidation on the Co K-edge.

during RWGS-CL. In addition, it is particularly noteworthy that the Co K-edge XANES spectra of Co–In_2O_3 (Fig. 4(C)) were peculiar. After the reduction, the spectrum was similar to that of Co-foil, but showed slightly different features (blue line in Fig. 4(C)). This spectrum indicated the formation of Co–In alloy in addition to Co metal. When the reduced Co–In_2O_3 was exposed to CO_2, the spectrum shifted to that of Co-foil (red lines in Fig. 4(C)). Results of XAFS measurements support the redox of indium with the formation and decomposition of Co–In alloys (detailed in the ESI† text). This redox mechanism might have contributed to the high redox performance of indium, especially its oxidation performance.

To investigate details of the difference in oxidation performance of Co–In_2O_3, kinetic analysis of the isothermal solid-state reaction proposed by Hancock and Sharp[29–31] was applied for the RWGS-CL oxidation step. Details of the method based on the kinetic model are described along with the fitting process in the ESI.† For In_2O_3, oxidation by CO_2 is known to proceed in the nucleation model.[12] In this model, the nuclei of the reaction are generated in the particles at the initial stage. The reaction proceeds as the nuclei grow and mutually collide continuously.[32–34] For In_2O_3, a rapid decrease in the reaction rate has been reported because of a decrease in the nucleation region in the initial stage of oxidation. Regarding the Co–In_2O_3, the oxidation reaction kinetics fitted best to the zero-order model.[29–31] This model is a reaction-order model in which the differential oxidation rate is kept constant irrespective of the degree of oxidation. Fig. 5 shows the differential oxidation rate behaviour of Co–In_2O_3. As presented in Fig. 5, the oxidation of Co–In_2O_3 progresses, while maintaining the differential oxidation rate up to solid conversion of about 50–60%, as expressed by the zero-order model. These results suggest that, in Co–In_2O_3, surface reaction sites with CO_2 do not decrease

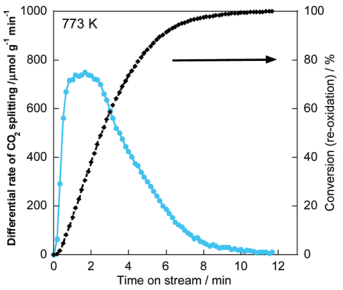

Fig. 5 Transition of differential oxidation rate on Co–In_2O_3.

with the progress of oxidation, *i.e.*, the oxide ions on the surface oxidized by CO_2 are regarded as migrating quickly to the bulk.

The rate constant k on the oxidation side at each temperature was calculated for the oxidation reaction of Co–In_2O_3. An Arrhenius plot was obtained (Fig. S6, ESI†). The reported apparent activation energy on the oxidation side of In_2O_3 is 85.9 kJ mol^{-1},[12] whereas 48.5 kJ mol^{-1} in Co–In_2O_3, indicating that the co-existence of Co reduces the activation barrier of the oxidation reaction of indium by about half.

Completion of quick oxidation in the Co–In_2O_3 might be realized by fast oxygen ion migration in the Co–In alloy. The schematic diagrams are portrayed in Fig. S7 (ESI†). Specifically, as found from structural analyses, Co–In_2O_3 gives Co–In alloys dispersed on In_2O_3 after the reduction. When the oxidation starts, CO_2 is adsorbed and dissociated on the Co–In alloy. Then oxide ions are supplied to the Co–In alloy surface. They quickly migrate from the Co–In alloy surface to the interface between the Co–In alloy and In_2O_3. This rapid migration of oxide ions into the bulk might engender the rapid growth of the In_2O_3. This peculiar oxidation mechanism gives Co–In_2O_3 a higher oxidation rate than those of materials described in earlier reports.

Conflicts of interest

The authors have no conflicts of interest.

References

1 IPCC AR6 Climate Change 2021: The *Physical Science Basis*.
2 S. J. Davis, K. Caldeira and H. D. Matthews, *Science*, 2010, **329**, 1330–1333.
3 F. V. Vázquez, J. Koponen, V. Ruuskanen, C. Bajamundi, A. Kosonen, P. Simell, J. Ahola, C. Frilund, J. Elfving, M. Reinikainen, N. Heikkinen, J. Kauppinen and P. Piermartini, *J. CO2 Util.*, 2018, **28**, 235–246.
4 I. Dimitriou, P. G. Gutiérrez, R. H. Elder, R. M. C. Franca, A. Azapagic and R. W. K. Allen, *Energy Environ. Sci.*, 2015, **8**, 1775–1789.
5 S. Perathoner and G. Centi, *ChemSusChem*, 2014, **7**, 1274–1282.
6 V. Dieterich, A. Buttler, A. Hanel, H. Spliethoff and S. Fendt, *Energy Environ. Sci.*, 2020, **13**, 3207–3252.
7 Y. A. Daza and J. N. Kuhn, *RSC Adv.*, 2016, **6**, 49675–49691.
8 D. S. Mallapragada, N. R. Singh, V. Curteanu and R. Agrawal, *Ind. Eng. Chem. Res.*, 2013, **52**, 5136–5144.
9 M. Wenzel, L. Rihko-Struckmann and K. Sundmacher, *AIChE J.*, 2015, **61**, 2–22.
10 M. Keller and J. Otomo, *J. CO2 Util.*, 2020, **40**, 101191.
11 Y. A. Daza, D. Maiti, R. A. Kent, V. R. Bhethanabotla and J. N. Kuhn, *Catal. Today*, 2015, **258**, 691–698.
12 J. Makiura, T. Higo, Y. Kurosawa, K. Murakami, S. Ogo, H. Tsuneki, Y. Hashimoto, Y. Sato and Y. Sekine, *Chem. Sci.*, 2021, **12**, 2108–2113.
13 Y. A. Daza, R. A. Kent, M. M. Yung and J. N. Kuhn, *Ind. Eng. Chem. Res.*, 2014, **53**, 5828–5837.
14 Y. A. Daza, D. Maiti, B. J. Hare, V. R. Bhethanabotla and J. N. Kuhn, *Surf. Sci.*, 2016, **648**, 92–99.
15 D. Maiti, B. J. Hare, Y. A. Daza, A. E. Ramos, J. N. Kuhn and V. R. Bhethanabotla, *Energy Environ. Sci.*, 2018, **11**, 648–659.
16 B. J. Hare, D. Maiti, Y. A. Daza, V. R. Bhethanabotla and J. N. Kuhn, *ACS Catal.*, 2018, **8**, 3021–3029.
17 B. L. Hare, D. Maiti, S. Ramani, A. E. Ramos, V. R. Bhethanabotla and J. N. Kuhn, *Catal. Today*, 2019, **323**, 225–232.
18 A. E. Ramos, D. Maiti, Y. A. Daza, J. N. Kuhn and V. R. Bhethanabotla, *Catal. Today*, 2019, **338**, 52–59.
19 B. J. Hare, D. Maiti, A. J. Meier, V. R. Bhethanabotla and J. N. Kuhn, *Ind. Eng. Chem. Res.*, 2019, **58**, 12551–12560.
20 M. Wenzel, N. V. R. A. Dharanipragada, V. V. Galvita, H. Poelman, G. B. Marin, L. Rihko-Struckmann and K. Sundmacher, *J. CO2 Util.*, 2017, **17**, 60–68.
21 M. Wenzel, L. Rihko-Struckmann and K. Sundmacher, *Chem. Eng. J.*, 2018, **336**, 278–296.
22 M. Najera, R. Solunke, T. Gardner and G. Veser, *Chem. Eng. Res. Des.*, 2011, **89**, 1533–1543.
23 N. V. R. A. Dharanipragada, L. C. Buelens, H. Poelman, E. D. Grave, V. V. Galvita and G. B. Marina, *J. Mater. Chem. A*, 2015, **3**, 16251–16262.
24 Y. Qiu, L. Ma, D. Zeng, M. Li, D. Cui, Y. Lv, S. Zhang and R. Xiao, *J. Energy Chem.*, 2020, **46**, 123–132.
25 L. Ma, Y. Qiu, M. Li, D. Cui, S. Zhang, D. Zeng and R. Xiao, *Ind. Eng. Chem. Res.*, 2020, **59**, 6924–6930.
26 V. V. Galvita, H. Poelman, V. Bliznuk, C. Detavernier and G. B. Marin, *Ind. Eng. Chem. Res.*, 2013, **52**, 8416–8426.
27 P. Kaiser, R. B. Unde, C. Kern and A. Jess, *Chem. Ing. Tech.*, 2013, **85**, 489–499.
28 J. P. Bros, M. Gaune-Escard, D. El Allam, R. Haddad and E. Hayer, *J. Alloys Compd.*, 1996, **233**, 264–271.
29 J. D. Hancock and J. H. Sharp, *J. Am. Ceram. Soc.*, 1972, **55**, 74–77.
30 K. Piotrowski, K. Mondal, H. Lorethova, L. Stonawski, T. Szymanski and T. Wiltowski, *Int. J. Hydrogen Energy*, 2005, **30**, 1543–1554.
31 Z. Zhou, L. Han and G. M. Bollas, *Int. J. Hydrogen Energy*, 2014, **39**, 8535–8556.
32 M. Avrami, *J. Chem. Phys.*, 1939, **7**, 1103–1112.
33 M. Avrami, *J. Chem. Phys.*, 1940, **8**, 212–224.
34 M. Avrami, *J. Chem. Phys.*, 1941, **9**, 177–184.

